Publication Year	2017
Acceptance in OA@INAF	2020-08-31T15:33:40Z
Title	Unveiling the early-stage anatomy of a protocluster hub with ALMA
Authors	Henshaw, J. D.; Jiménez-Serra, I.; Longmore, S. N.; Caselli, P.; Pineda, J. E.; et al.
DOI	10.1093/mnrasl/slw154
Handle	http://hdl.handle.net/20.500.12386/27004
Journal	MONTHLY NOTICES OF THE ROYAL ASTRONOMICAL SOCIETY
Number	464

Monthly Notices
of the
ROYAL ASTRONOMICAL SOCIETY

MNRAS **464,** L31–L35 (2017) doi:10.1093/mnrasl/slw154
Advance Access publication 2016 August 1

Unveiling the early-stage anatomy of a protocluster hub with ALMA

J. D. Henshaw,[1,2★] I. Jiménez-Serra,[3,4] S. N. Longmore,[1] P. Caselli,[5] J. E. Pineda,[5] A. Avison,[6,7] A. T. Barnes,[1,5] J. C. Tan[8] and F. Fontani[9]

[1] *Astrophysics Research Institute, Liverpool John Moores University, Liverpool L3 5RF, UK*
[2] *School of Physics and Astronomy, University of Leeds, Leeds LS2 9JT, UK*
[3] *School of Physics and Astronomy, Queen Mary University of London, Mile End Road, London E1 4NS*
[4] *University College London, 132 Hampstead Road, London NW1 2PS, UK*
[5] *Max-Planck Institute for Extraterrestrial Physics, Giessenbachstrasse 1, D-85748 Garching, Germany*
[6] *Jodrell Bank Centre for Astrophysics, School of Physics and Astronomy, The University of Manchester, Manchester M13 9PL, UK*
[7] *UK ALMA Regional Centre Node, Manchester M13 9PL, UK*
[8] *Departments of Astronomy and Physics, University of Florida, Gainesville, FL 32611, USA*
[9] *INAF–Osservatorio Astrofisico di Arcetri, Largo E. Fermi 5, I-50125 Firenze, Italy*

Accepted 2016 July 28. Received 2016 July 27; in original form 2016 June 27

ABSTRACT

High-mass stars shape the interstellar medium in galaxies, and yet, largely because the initial conditions are poorly constrained, we do not know how they form. One possibility is that high-mass stars and star clusters form at the junction of filamentary networks, referred to as 'hubs'. In this Letter we present the complex anatomy of a protocluster hub within an Infrared Dark Cloud (IRDC), G035.39−00.33, believed to be in an early phase of its evolution. We use high-angular resolution ($\{\theta_{\rm maj}, \theta_{\rm min}\} = \{1.4\,{\rm arcsec}, 0.8\,{\rm arcsec}\} \sim \{0.02\,{\rm pc}, 0.01\,{\rm pc}\}$) and high-sensitivity (0.2 mJy $\rm beam^{-1}$; $\sim$0.2 $\rm M_{\odot}$) 1.07 mm dust continuum observations from the Atacama Large Millimeter Array (ALMA) to identify a network of narrow, 0.028 ± 0.005 pc wide, filamentary structures. These are a factor of $\gtrsim$3 narrower than the proposed 'quasi-universal' $\sim$0.1 pc width of interstellar filaments. Additionally, 28 compact objects are reported, spanning a mass range $0.3\,{\rm M_{\odot}} < M_{\rm c} < 10.4\,{\rm M_{\odot}}$. This indicates that at least some low-mass objects are forming coevally with more massive counterparts. Comparing to the popular 'bead-on-a-string' analogy, the protocluster hub is poorly represented by a monolithic clump embedded within a single filament. Instead, it comprises multiple intra-hub filaments, each of which retains its integrity as an independent structure and possesses its own embedded core population.

Key words: stars: formation – stars: massive – ISM: clouds – ISM: individual: G035.39–00.33 – ISM: structure.

1 INTRODUCTION

In recent years, Infrared Dark Clouds (IRDCs; Pérault et al. 1996; Egan et al. 1998) have received significant attention in the field of high-mass (>8 $\rm M_{\odot}$) star formation, owing to their natal association with massive ($\sim$100 $\rm M_{\odot}$) protocluster clumps. Early studies earmarked IRDC clumps as potential locations of high-mass star and star cluster formation (e.g. Rathborne, Jackson & Simon 2006), with high-angular resolution observations adding credence to this theory (Tan et al. 2013, 2016; Cyganowski et al. 2014; Zhang et al. 2015).

Common to many IRDCs is the presence of filamentary structure. As a key ingredient of the molecular interstellar medium (André et al. 2010; Molinari et al. 2010), there has been a commensurate drive towards understanding the intrinsic nature of filaments. Physically, interstellar filaments are characterized by a 'quasi-universal' width of the order $\sim$0.1 pc (Arzoumanian et al. 2011). The origin of this commonly observed width is currently unknown. One possibility is that this scale is a direct reflection of the physics of filament formation, following the dissipation of turbulent energy via shocks at the stagnation points of a turbulent velocity field (e.g. Federrath 2016). From a dynamical perspective, both observations (e.g. Schneider et al. 2012) and simulations (Dale & Bonnell 2011; Myers et al. 2013; Gómez & Vázquez-Semadeni 2014) agree that filaments play an important role in star and cluster formation. In this context, filaments may act as tributaries, funnelling mass towards protocluster clumps at the centre of so-called hub-filament systems (Myers 2009; Liu et al. 2012; Gómez & Vázquez-Semadeni 2014; Smith et al. 2016).

Observational studies of relatively evolved massive star-forming clusters support the 'hub-filament' scenario for high-mass star and star cluster formation (e.g. Liu et al. 2012). For objects at an early stage of evolution, such as IRDCs, there is growing evidence in the

---

★ E-mail: j.d.henshaw@ljmu.ac.uk

© 2016 The Authors
Published by Oxford University Press on behalf of the Royal Astronomical Society

form of coherent, parsec-scale, velocity gradients associated with prominent filaments in the vicinity of protocluster clumps (Peretto et al. 2014; Tackenberg et al. 2014). Although high-angular resolution observations of IRDC clumps exist, these often focus on the embedded core population (e.g. Wang et al. 2014; Beuther et al. 2015), and typically lack enough spatial coverage and dynamic range to obtain a global understanding of the anatomy of hub-filament systems. As a consequence, the physical structure of protocluster hubs during the earliest phases of evolution is poorly documented. It remains unknown, for example, whether filamentary structures exist internally within hubs, and if so, what role they may play in the subsequent evolution of protocluster cores.

In this Letter we present high-angular resolution ($\{\theta_{\rm maj}, \theta_{\rm min}\} = \{1.4\,{\rm arcsec}, 0.8\,{\rm arcsec}\}$; see Section 2) and high-sensitivity (0.2 mJy beam^{-1}) Atacama Large Millimetre Array (ALMA) cycle 2 dust continuum observations towards a $\sim$100 M$_\odot$ clump (Rathborne et al. 2006; Butler & Tan 2012), H6 (referred to as MM7 in Rathborne et al. 2006), located within the IRDC G035.39−00.33 (cloud H; Butler & Tan 2012). This cloud is reasonably massive ($\sim 2 \times 10^4$ M$_\odot$ at a kinematic distance of 2.9 kpc; Simon et al. 2006; Kainulainen & Tan 2013) and comprises a network of kinematically identified sub-filaments that overlap spatially at the location of the H6 hub (Henshaw et al. 2013, 2014; Jiménez-Serra et al. 2014). Combining ALMA observations with those from the Atacama Compact Array (ACA), allows us to recover extended structures inside the hub, and unveil a network of narrow intra-hub filaments and embedded structure that had previously remained elusive.

2 OBSERVATIONS

ALMA cycle 2 Band 7 observations were carried out towards the H6 hub (project: 2013.1.01035.S, PI: Henshaw) using the 12 m ALMA and 7 m ACA arrays. The precipitable water vapour (PWV) was 1.53 mm, resulting in system temperatures of $\sim$130 K. Primary beam sizes of the 12 m and 7 m antennas at 279 GHz are $\sim$22 arcsec and 38 arcsec, respectively. A 7-field mosaic was used to cover a region $\sim$40 arcsec × 40 arcsec (corresponding to 0.55 pc × 0.55 pc). The 12 m mosaic can be seen as white open circles in Fig. 1, which shows the *Spitzer* Infrared Array Camera (IRAC) 8 µm image of G035.39−00.33, from the Galactic Legacy Mid-Plane Survey Extraordinaire (GLIMPSE; Churchwell et al. 2009). The shortest available baseline from the 7 m array was $D = 9$ m. We are therefore sensitive to emission on scales up to $\sim$30 arcsec ($\sim$0.4 pc). For the 12 m observations, quasars J1924-2914 and J1851+0035 were used for bandpass and time-dependent gain calibration (with measurements every $\sim$10 min), respectively. Flux calibration was performed using Neptune. The spectral setup included a 1.875 GHz continuum band centred on 277.5 GHz. The 12 m and 7 m visibility data were combined and imaged in CASA. Imaging and deconvolution was performed using Multi-Scale CLEAN with natural weighting. The resultant synthesized beam is $\{\theta_{\rm maj}, \theta_{\rm min}\} = \{1.4\,{\rm arcsec}, 0.8\,{\rm arcsec}\} \sim \{0.02\,{\rm pc}, 0.01\,{\rm pc}\} \sim \{4000\,{\rm au}, 2000\,{\rm au}\}$ with a position angle P. A. $= -57\overset{\circ}{.}9$. The continuum image reaches a $1\sigma_{\rm rms}$ noise level of 0.2 mJy beam^{-1} (estimated from emission-free regions after primary beam correction). From the Rathborne et al. (2006) 1.2 mm dust continuum image of the H6 clump (size $\sim$40 arcsec, $\sim$ to the extent of our ALMA mosaic), we estimate that the integrated flux at 1.07 mm is $\sim$0.8 Jy (assuming a dust emissivity index, $\beta = 1.75$). The total flux in our ALMA image is $\sim$0.5 Jy, indicating that we recover about 60 per cent of the total flux.

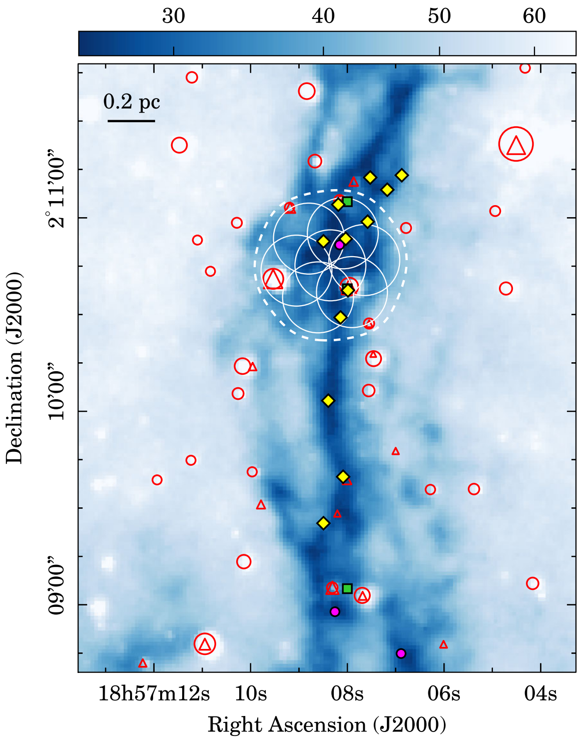

Figure 1. *Spitzer* 8 µm image of G035.39−00.33 (Churchwell et al. 2009), with logarithmic intensity scale in units of MJy sr^{-1}. Open white circles indicate the 7-field 12 m ALMA mosaic. The dashed contour displays the edge of the ALMA mosaic. Filled yellow diamonds and filled magenta circles indicate the locations of 3.2 mm PdBI cores identified by Henshaw et al. (2016) and high-mass cores reported by Butler & Tan (2012), respectively. Open red circles and red triangles refer to the 8 µm, and 24 µm emission, respectively (Carey et al. 2009; Jiménez-Serra et al. 2010). The symbol sizes are scaled by the source flux. Filled green squares highlight the location of extended 4.5 µm emission (Chambers et al. 2009).

3 RESULTS

The ALMA 1.07 mm dust continuum emission map of the H6 region is displayed in the left-hand panel of Fig. 2. This new high-angular resolution and high-sensitivity map reveals a striking network of intra-hub filaments, which had remained elusive in previous observations (e.g. Henshaw et al. 2016).

The filamentary structures evident in Fig. 2 are narrow in comparison to the prominent filament seen in extinction in Fig. 1 and to the 'quasi-universal' filament width of $\sim$0.1 pc (Arzoumanian et al. 2011; André et al. 2016). We can estimate the width of these filaments via the analysis of their radial surface density profiles, $\Sigma_{\rm f}(r)$. We focus on the filament marked 'F' in Fig. 2, as it exhibits the most uniform structure of those observed. To derive the radial surface density profile we rotate the image and take horizontal slices of equivalent breadth across the filament crest. The column density, $N_{\rm H}$, is estimated using the following assumptions: (i) the dust continuum emission is optically thin; (ii) a total (gas plus dust)-to-dust-mass ratio, $R_{\rm gd} = 141$ (Draine 2011); (iii) a dust opacity per unit mass, $\kappa_\nu \approx 1.26$ cm^{2}g^{-1} (valid for the moderately coagulated thin ice mantle dust model of Ossenkopf & Henning 1994, assuming $\beta = 1.75$); (iv) a dust temperature, $T_{\rm d} = 13$ K. For an in-depth discussion on these considerations, please see Henshaw et al. (2016). After accounting for uncertainties in our assumed parameters, the uncertainty in $N_{\rm H}$ is $\sim$50 per cent. The resultant $1\sigma_{\rm rms}$ sensitivity is $\sim 4 \times 10^{22}$ cm^{-2}.

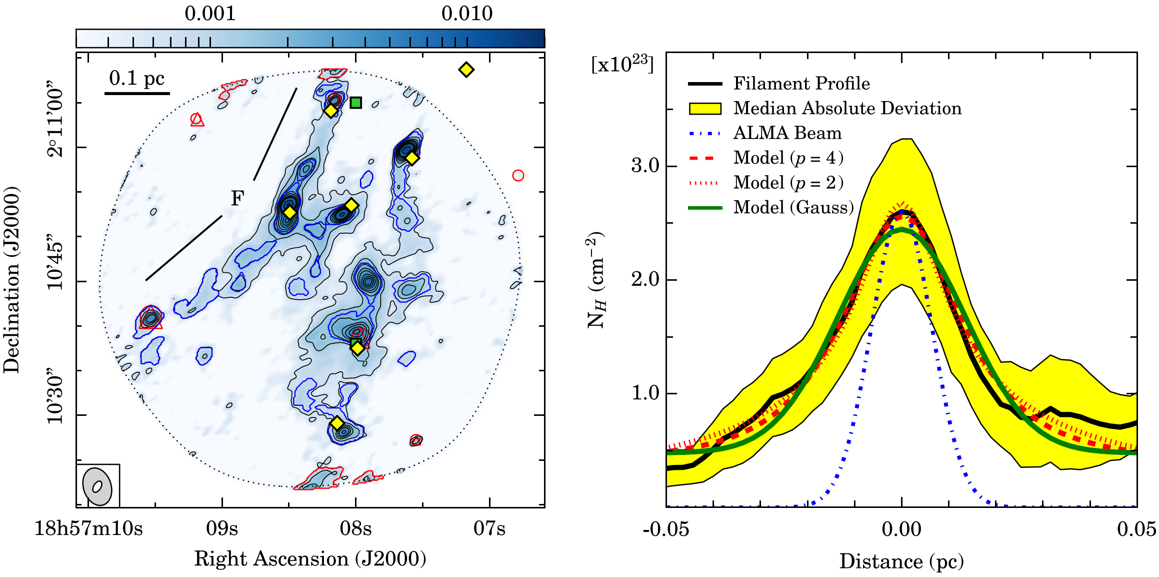

Figure 2. Left: the ALMA 1.07 mm continuum map (logarithmic colour scale in units of Jy beam^{-1} and thin black contours). Contours increase in $3\sigma_{\rm rms}$ ($\sigma_{\rm rms} \sim 0.2$ mJy beam^{-1}) steps from $3\sigma_{\rm rms}$ to $15\sigma_{\rm rms}$, then in $5\sigma_{\rm rms}$ steps up until $30\sigma_{\rm rms}$, before increasing in $20\sigma_{\rm rms}$ steps until $70\sigma_{\rm rms}$ ($\sim$0.15 Jy beam^{-1}). The symbols and dotted contour have equivalent meaning to those presented in Fig. 1. The thick blue and red contours depict identified sources (Section 3 and Table 1), with the latter representing leaves that are rejected from further analysis as they reside at the very edge of the map. The PdBI (Henshaw et al. 2016) and ALMA synthesized beams are shown in the bottom left-hand corner in grey and white, respectively. Right: the median column density profile perpendicular to the filament marked 'F' in the left-hand panel (thick black line). The yellow area indicates the median absolute deviation. The ALMA synthesized beam is indicated by the blue line. Different models used to derive the filament width are shown in red and green (see Section 3 for more details).

We follow a conservative approach to estimating the filament width, using the median, rather than mean surface density profile (as is more commonly used). The presence of embedded cores means that the mean surface density profile typically yields narrower filaments. For completeness however, we derive the filament width using both profiles. The median radial surface density profile of the filament marked 'F' in left-hand panel of Fig. 2 is presented in the right-hand panel.

Two independent models are used to establish the filament width (Smith, Glover & Klessen 2014; Federrath 2016). First we consider the filament as an idealized cylinder, the surface density profile of which can be described by a Plummer profile of the form

$$\Sigma_{\rm f}(r) = A_p \frac{\Sigma_{\rm f,0}}{[1+(r/R_{\rm flat})^2]^{\frac{p-1}{2}}} + \Sigma_{\rm bg}, \tag{1}$$

where r refers to the cylinder radius, A_p is a finite constant factor dependent on the density profile power-law index, p, and the filament inclination angle, i (for simplicity we assume $i = 0$), $\Sigma_{\rm f,0} = \rho_{\rm f,0}R_{\rm flat}$, where $\rho_{\rm f,\,0}$ is the filament central density and $R_{\rm flat}$ is the radius of the flat inner section of the cylinder. For $p = 2$, the filament width is $W_{\rm f} \sim 3R_{\rm flat}$ (Arzoumanian et al. 2011). The second model involves fitting a simple Gaussian profile of the form

$$\Sigma_{\rm f}(r) = \Sigma_{\rm f,0}{\rm exp}\left(-\frac{r^2}{2\sigma^2_{\rm Gauss}}\right) + \Sigma_{\rm bg}, \tag{2}$$

where $\sigma_{\rm Gauss}$ is the surface density dispersion about the filament centre and the width is given by $W_{\rm f} = 2(2\ln 2)^{1/2}\,\sigma_{\rm Gauss}$.

In Fig. 2 we show the best-fitting model solutions to the radial column density profile. The models described by equation (1) are shown in red. The dashed and dotted lines are the solutions assuming $p = 4$ and $p = 2$, respectively, where the former is the Ostriker (1964) solution for an isothermal filament in hydrostatic equilibrium. The Gaussian model is shown in green. From Fig. 2, a Plummer-like surface density profile appears to better represent the observations, particularly within ±0.01 pc and for radial distances <-0.02 pc and >0.02 pc. Taking $p = 2$ (equation 1), we find $R_{\rm flat} = 0.009 \pm 0.001$ pc. The resultant width is $W_{\rm f} \approx 0.027 \pm 0.006$ pc. To investigate the possibility of variation in the filament width, we also fit individual profiles. From a sample of $\sim$150 radial cuts, we find a mean width of $W_{\rm f} \approx 0.029 \pm 0.013$ pc (where the uncertainty reflects the standard deviation). Alternatively, the Gaussian model returns a full-width at half-maximum width, after beam deconvolution, of $W_{\rm f} \approx 0.028 \pm 0.005$ pc.[1]

Our ALMA continuum image also reveals the presence of 28 high-contrast, compact cores embedded within the filaments. In Fig. 1 and Fig. 2 (left-hand panel), yellow diamonds indicate the position of the 3.2 mm continuum sources previously identified with the Plateau de Bure Interferometer (PdBI; Henshaw et al. 2016). This comparison shows that a greater number of objects (28 versus 7) are detected in this new image due to the high angular resolution, sensitivity and dynamic range of ALMA.

To characterize the physical properties of the compact cores, we use ASTRODENDRO to first extract the sources.[2] The thick blue and red contours in the left-hand panel of Fig. 2 show the locations of the 28 identified dendrogram leaves (the highest level in the dendrogram hierarchy, representing the smallest structures identified). Out of these leaves, four are rejected from further analysis as they reside at the very edge of the mosaic (thick red contours).

The derived equivalent radii of the leaves range between $0.01\,{\rm pc} < R_{\rm eq} < 0.03\,{\rm pc}$, with a mean value of $\sim$0.02 pc

---

[1] Using the mean column density profile gives widths of $W_{\rm f} \approx 0.021$ pc or 0.020 pc for the Plummer and Gaussian models, respectively.

[2] The following parameters are used in computing the dendrogram: `min_value` = $3\sigma_{\rm rms}$; `min_delta` = $1\sigma_{\rm rms}$; `min_npix` = 60.

Table 1. Dendrogram leaves: physical properties (see Section 3).

RA[a]	Dec[a]	$R_{\rm eq}$[b] (pc)	$N_{\rm H,\,c}$[c] $\times\ 10^{23}$ ($\rm cm^{-2}$)	$M_{\rm c}$[d] ($\rm M_{\odot}$)	$n_{\rm H,\,c,\,eq}$[e] $\times\ 10^{6}$ ($\rm cm^{-3}$)	$t_{\rm ff,\,c}$[f] $\times\ 10^{4}$ (yr)
18:57:08.09	2:10:28.05	0.026	8.3	3.1	1.2	4.0
18:57:08.43	2:10:31.65	0.019	2.1	1.0	1.0	4.3
18:57:08.06	2:10:33.00	0.013	1.9	0.4	1.4	3.7
18:57:07.62	2:10:36.15	0.011	1.7	0.3	1.5	3.5
18:57:09.13	2:10:36.60	0.013	2.5	0.5	1.5	3.5
18:57:09.50	2:10:38.10	0.017	2.0	0.7	1.0	4.4
18:57:08.00	2:10:39.30	0.031	10.6	7.7	1.8	3.3
18:57:09.53	2:10:40.80	0.021	7.7	2.2	1.5	3.6
18:57:09.23	2:10:41.70	0.026	2.4	1.9	0.7	5.1
18:57:07.61	2:10:43.95	0.023	4.4	2.3	1.3	3.8
18:57:08.46	2:10:44.40	0.014	2.1	0.6	1.6	3.5
18:57:08.88	2:10:44.55	0.012	3.4	0.6	2.7	2.6
18:57:07.91	2:10:45.00	0.024	13.9	5.6	2.9	2.6
18:57:08.30	2:10:46.20	0.010	2.9	0.4	3.2	2.4
18:57:08.67	2:10:48.60	0.019	3.1	1.6	1.6	3.5
18:57:08.31	2:10:51.00	0.014	3.9	1.2	3.1	2.5
18:57:07.62	2:10:51.75	0.021	2.5	1.5	1.1	4.2
18:57:08.10	2:10:52.50	0.018	21.5	4.4	5.3	1.9
18:57:08.50	2:10:53.55	0.026	28.3	10.4	4.1	2.1
18:57:07.91	2:10:56.55	0.011	1.7	0.3	1.5	3.5
18:57:08.37	2:10:57.60	0.014	6.3	1.5	4.2	2.1
18:57:07.62	2:10:59.70	0.027	26.2	6.7	2.2	2.9
18:57:08.16	2:11:05.25	0.016	7.5	1.6	2.5	2.8
18:57:08.26	2:11:06.45	0.011	2.4	0.4	2.2	2.9

[a] Position of peak emission.

[b] Equivalent radius, $R_{\rm eq} = (N_{\rm pix}A_{\rm pix}/\pi)^{1/2}$.

[c] Peak beam-averaged column density. Uncertainty: $\sigma N_{\rm H,\,c} \sim 50$ per cent.

[d] Leaf mass. Uncertainty: $\sigma M_{\rm c} \sim 60$ per cent.

[e] Leaf number density. Uncertainty: $\sigma n_{\rm H,\,c,\,eq} \sim 75$ per cent.

[f] Leaf free-fall time. Uncertainty: $\sigma t_{\rm ff,\,c} \sim 40$ per cent.

($R_{\rm eq} \equiv N_{\rm pix}A_{\rm pix}/\pi$, where $N_{\rm pix}$ is the total number of pixels and $A_{\rm pix}$ is the area of a single 0.15 arcsec × 0.15 arcsec pixel). The mean angular separation of the leaves is ∼4.6 arcsec, which corresponds to a projected linear separation of ∼0.065 pc at the distance of G035.39−00.33. Leaf peak beam-averaged column densities and masses are estimated following the assumptions listed above (subscript ‘c’ is used to distinguish the core properties from the filament properties discussed above). Under these assumptions the derived peak beam-averaged column densities of the leaves range from $0.2 \times 10^{24}\ {\rm cm^{-2}} < N_{\rm H,\,c} < 2.8 \times 10^{24}\ {\rm cm^{-2}}$. Leaf masses range from $0.3\ {\rm M_{\odot}} < M_{\rm c} < 10.4\ {\rm M_{\odot}}$ (the uncertainty in our mass estimate is ∼60 per cent and our estimated mass sensitivity is $\sim 0.2\ {\rm M_{\odot}}$), which extends the distribution of detected core masses to lower values with respect to that derived by Henshaw et al. (2016, core masses ranging from ∼8 to 26 $\rm M_{\odot}$). Estimating the mass within the boundaries of the leaves identified by Henshaw et al. (2016) from our ALMA image, we note a ∼30 per cent reduction, on average (although this can be ∼60 per cent). This difference is likely due to the fact that the ALMA and PdBI images are sensitive to different spatial scales, and/or variation in the dust properties at the respective resolution of the two images. The equivalent number densities for each leaf, $n_{\rm H,c,eq}$ (i.e. the density of a structure with mass, $M_{\rm c}$, and radius, $R_{\rm eq}$, assuming spherical geometry), range from $0.7 \times 10^{6}\ {\rm cm^{-3}}$ to $5.3 \times 10^{6}\ {\rm cm^{-3}}$ and the corresponding range in the estimated free-fall time is 1.9×10^{4} yr to 5.1×10^{4} yr. All derived values can be found in Table 1, where the leaves are listed in order of increasing declination.

4 THE EARLY-STAGE ANATOMY OF A PROTOCLUSTER HUB

Observational studies of molecular gas kinematics in both low-mass and high-mass star-forming regions have reported the presence of large-scale (∼2 pc) velocity gradients in hub-filament systems (Liu et al. 2012; Kirk et al. 2013; Peretto et al. 2013, 2014; Tackenberg et al. 2014), possibly indicating mass transport (e.g. Gómez & Vázquez-Semadeni 2014). In this scenario, protocluster clumps (analogous to ‘beads-on-a-string’) grow in mass as material is accreted from parsec-scales along tributary filaments. Alternatively, recent single-dish and interferometric observations have revealed that, in some cases, these velocity ‘gradients’ may instead be caused by the deceptive superposition of underlying substructure (e.g. Hacar et al. 2013; Henshaw et al. 2014). In such instances, a centralized ‘hub’ may represent the location where several sub-filaments, gathered together by large-scale motions, spatially overlap and merge (as inferred from e.g. the hydrodynamical simulations of Smith et al. 2016). Comparing to the ‘bead-on-a-string’ analogy, where the protocluster hub is represented as large bead on a single string, each sub-filament in the latter scenario retains its integrity as an independent structure within the ‘hub’ and possesses its own core population.

The results presented in Section 3 support the latter of these two scenarios. The anatomy of the H6 protocluster, at this early phase of its evolution, consists of several spatially resolved intra-hub filaments, each with an associated population of embedded compact cores. This is consistent with both the kinematic and fragmentation analyses presented by Henshaw et al. (2014, 2016), respectively.

With widths of ∼0.028 ± 0.005 pc (Section 3), the H6 filaments are remarkably narrower than the proposed ‘quasi-universal’ width of interstellar filaments (∼0.1 pc), a phenomenon which is supposedly independent of column density, evolutionary stage, and star formation efficiency (Arzoumanian et al. 2011; Federrath 2016). Although there are several examples in the literature of filaments displaying a range of widths, rather than displaying a characteristic value (Pineda et al. 2011; Hennemann et al. 2012; Juvela et al. 2012; Schisano et al. 2014), it has been proposed that the width of filaments is intrinsically linked to their formation in shocks, and that this width may be set by the sonic scale of molecular cloud turbulence, $\lambda_{\rm sonic}$ (Arzoumanian et al. 2011; Federrath 2016). This scale represents the transition from supersonic to subsonic turbulence and is given by (Federrath 2016):

$$\lambda_{\rm sonic} = L\left[\frac{c_{\rm s}}{\sigma_{\upsilon,\rm 3D}}(1+\beta^{-1})\right]^{2}, \tag{3}$$

where L is the cloud scale, $c_{\rm s} = (k_{\rm B}T/\mu m_{\rm H})^{1/2}$ is the isothermal sound speed at a gas temperature T, $\sigma_{\upsilon,\rm 3D}$ is the 3D velocity dispersion on the cloud scale, and $\beta = 2c_{\rm s}^{2}/\upsilon_{\rm A}^{2}$ is the ratio of thermal to magnetic pressure ($\upsilon_{\rm A} = B/\sqrt{4\pi\rho_{\rm f}}$ is the Alfvén velocity).

By excluding the effects of magnetic fields from equation (3) (i.e. $\beta \rightarrow \infty$), we can estimate the corresponding sonic scale for the molecular gas in the H6 hub. Assuming that $T = 13$ K (see Section 3), $\sigma_{\upsilon,\rm 3D} \approx \sqrt{3}\sigma_{\upsilon,\rm 1D} \approx 0.7\ {\rm km\,s^{-1}}$ (the mean value derived from line-fitting; Henshaw et al. 2014), and $L = 0.35$ pc (the projected extent of the filament in Fig. 2), we find a sonic scale $\lambda_{\rm sonic} \approx 0.03$ pc, in agreement with our derived filament width. Although the ‘cloud scale’ (i.e. L) used above is somewhat dependant, in this simplistic analysis, on the field of view of our ALMA mosaic, this could imply that the observed intra-hub filaments have formed following the dissipation of turbulent energy via shocks. However, if the width of the H6 filament is indeed set by the sonic scale, then one would expect to observe a direct transition to coherence across the filament boundary similar to that reported by Pineda et al. (2010) in the Barnard 5 core in Perseus. This prospect will be investigated, along with a detailed description of the intra-hub kinematics in a future publication (Henshaw et al., in preparation).

Our ALMA observations also reveal a number of cores associated with the sub-filaments, spanning a range of masses between $0.3\,\mathrm{M}_{\odot} < M_{\rm c} < 10.4\,\mathrm{M}_{\odot}$. Previous studies of G035.39−00.33 had reported a lack of cores in the mass range 2–8 $\mathrm{M}_{\odot}$ (Henshaw et al. 2016). A similar result was obtained by Zhang et al. (2015), studying the P1 clump in IRDC G28.34+0.06, who reported a dearth of low-mass cores (by a factor of 5) in the 1–2 $\mathrm{M}_{\odot}$ mass range. With only 24 cores identified in this study, we are unable to establish a robust statistical determination of the mass function in the H6 hub. However, with this new image, we identify a number of low-mass cores within the 2–8 $\mathrm{M}_{\odot}$ mass range. We therefore conclude that the previously reported dearth of such low-mass objects may be of observational, rather than physical origin, and that at least some low-mass cores are forming coevally in the immediate neighbourhood of more massive objects. The differences in the core mass distribution function between G035.39−00.33 and G28.34+0.06 may be due to either an evolutionary effect (where the latter is at a more evolved phase in its evolution, as suggested by the several molecular outflows reported in the P1 clump) or, as discussed by Zhang et al. (2015), because the lower mass cores in G28.34+0.06 are forming within the immediate vicinity of higher mass objects. In this latter scenario, the low-mass objects may be indistinguishable from the extended emission of the P1 star-forming ridge.

In summary, the high-angular resolution ($\sim$0.01 pc) and high-sensitivity ($\sim$0.2 mJy beam^{-1}) observations of the H6 clump have enabled us to investigate the anatomy of this complex protocluster hub with a high-degree of precision. Previously unresolved narrow (0.028 ± 0.005 pc) intra-hub filaments are revealed, as well as a number of low- and intermediate-mass cores. Although this study is insufficient to conclude that the detected narrow filaments (and their associated cores) are an intrinsic constituent of the initial phases of intermediate- and/or high-mass star formation, we have clearly demonstrated the need for high-angular resolution, high-sensitivity and high-dynamic range observations in determining the anatomy of such regions. Future investigations will focus on the complex gas dynamics of this region, with the aim of understanding how prestellar cores attain their mass during the early phases of evolution in protocluster hubs.

ACKNOWLEDGEMENTS

We thank the anonymous referee for their comments and Nate Bastian for helpful discussions. This Letter makes use of the following ALMA data: ADS/JAO.ALMA#2013.1.01035.S. ALMA is a partnership of ESO (representing its member states), NSF (USA) and NINS (Japan), together with NRC (Canada), NSC and ASIAA (Taiwan), and KASI (Republic of Korea), in cooperation with the Republic of Chile. The Joint ALMA Observatory is operated by ESO, AUI/NRAO and NAOJ. IJ-S acknowledges the financial support received from the STFC through an Ernest Rutherford Fellowship (proposal number ST/L004801/1). PC and JEP acknowledge support from European Research Council (ERC; project PALs 320620). JCT acknowledges NASA grant ADAP10-0110. This research has benefitted from the ASTROPY (Astropy Collaboration et al. 2013), MATPLOTLIB (Hunter 2007), and ASTRODENDRO (www.dendrograms.org) software packages.

REFERENCES

André P. et al., 2010, A&A, 518, L102
André P. et al., 2016, A&A, 592, A54
Arzoumanian D. et al., 2011, A&A, 529, L6
Astropy Collaboration, et al., 2013, A&A, 558, A33
Beuther H. et al., 2015, A&A, 581, A119
Butler M. J., Tan J. C., 2012, ApJ, 754, 5
Carey S. J. et al., 2009, PASP, 121, 76
Chambers E. T., Jackson J. M., Rathborne J. M., Simon R., 2009, ApJS, 181, 360
Churchwell E. et al., 2009, PASP, 121, 213
Cyganowski C. J. et al., 2014, ApJ, 796, L2
Dale J. E., Bonnell I., 2011, MNRAS, 414, 321
Draine B. T., 2011, Physics of the Interstellar and Intergalactic Medium. Princeton Univ. Press, Princeton, NJ
Egan M. P., Shipman R. F., Price S. D., Carey S. J., Clark F. O., Cohen M., 1998, ApJ, 494, L199
Federrath C., 2016, MNRAS, 457, 375
Gómez G. C., Vázquez-Semadeni E., 2014, ApJ, 791, 124
Hacar A., Tafalla M., Kauffmann J., Kovács A., 2013, A&A, 554, A55
Hennemann M. et al., 2012, A&A, 543, L3
Henshaw J. D., Caselli P., Fontani F., Jiménez-Serra I., Tan J. C., Hernandez A. K., 2013, MNRAS, 428, 3425
Henshaw J. D., Caselli P., Fontani F., Jiménez-Serra I., Tan J. C., 2014, MNRAS, 440, 2860
Henshaw J. D. et al., 2016, preprint (arXiv:1607.07452)
Hunter J. D., 2007, Comput. Sci. Eng., 9, 90
Jiménez-Serra I., Caselli P., Tan J. C., Hernandez A. K., Fontani F., Butler M. J., van Loo S., 2010, MNRAS, 406, 187
Jiménez-Serra I., Caselli P., Fontani F., Tan J. C., Henshaw J. D., Kainulainen J., Hernandez A. K., 2014, MNRAS, 439, 1996
Juvela M. et al., 2012, A&A, 541, A12
Kainulainen J., Tan J. C., 2013, A&A, 549, A53
Kirk H., Myers P. C., Bourke T. L., Gutermuth R. A., Hedden A., Wilson G. W., 2013, ApJ, 766, 115
Liu H. B., Jiménez-Serra I., Ho P. T. P., Chen H.-R., Zhang Q., Li Z.-Y., 2012, ApJ, 756, 26
Molinari S. et al., 2010, A&A, 518, L100
Myers P. C., 2009, ApJ, 700, 1609
Myers A. T., McKee C. F., Cunningham A. J., Klein R. I., Krumholz M. R., 2013, ApJ, 766, 97
Ossenkopf V., Henning T., 1994, A&A, 291, 943
Ostriker J., 1964, ApJ, 140, 1056
Pérault M. et al., 1996, A&A, 315, L165
Peretto N. et al., 2013, A&A, 555, A112
Peretto N. et al., 2014, A&A, 561, A83
Pineda J. E., Goodman A. A., Arce H. G., Caselli P., Foster J. B., Myers P. C., Rosolowsky E. W., 2010, ApJ, 712, L116
Pineda J. E. et al., 2011, ApJ, 743, 201
Rathborne J. M., Jackson J. M., Simon R., 2006, ApJ, 641, 389
Schisano E. et al., 2014, ApJ, 791, 27
Schneider N. et al., 2012, A&A, 540, L11
Simon R., Rathborne J. M., Shah R. Y., Jackson J. M., Chambers E. T., 2006, ApJ, 653, 1325
Smith R. J., Glover S. C. O., Klessen R. S., 2014, MNRAS, 445, 2900
Smith R. J., Glover S. C. O., Klessen R. S., Fuller G. A., 2016, MNRAS, 455, 3640
Tackenberg J. et al., 2014, A&A, 565, A101
Tan J. C., Kong S., Butler M. J., Caselli P., Fontani F., 2013, ApJ, 779, 96
Tan J. C., Kong S., Zhang Y., Fontani F., Caselli P., Butler M. J., 2016, ApJ, 821, L3
Wang K. et al., 2014, MNRAS
Zhang Q., Wang K., Lu X., Jiménez-Serra I., 2015, ApJ, 804, 141

This paper has been typeset from a TEX/LATEX file prepared by the author.